16 x 25 Ge:Ga Detector Arrays for FIFI LS

D. Rosenthal[a], J. W. Beeman[b], N. Geis[a], L. Looney[a],
A. Poglitsch[a], W. K. Park[a], W. Raab[a], A. Urban[a]

[a]Max-Planck-Institut für Extraterrestrische Physik, D-85740 Garching, Germany
[b]Lawrence Berkeley National Laboratory, Berkeley, CA 94720

ABSTRACT

We are developing two-dimensional 16×25 pixel detector arrays of both unstressed and stressed Ge:Ga photoconductive detectors for far-infrared astronomy from SOFIA. The arrays, based on earlier 5×5 detector arrays used on the KAO, will be for our new instrument, the Far Infrared Field Imaging Line Spectrometer (FIFI LS). The unstressed Ge:Ga detector array will cover the wavelength range from 40 to 120 μm, and the stressed Ge:Ga detector array from 120 to 210 μm. The detector arrays will be operated with multiplexed integrating amplifiers with cryogenic readout electronics located close to the detector arrays. The design of the stressed detector array and results of current measurements on several prototype 16 pixel linear arrays will be reported. They demonstrate the feasibility of the current concept.

Keywords: stressed Ge:Ga detectors, FIR, FIFI LS, SOFIA

1. INTRODUCTION

For the Far Infrared Field Imaging Line Spectrometer (FIFI LS),[1–3] we need two-dimensional 16×25 pixel detector arrays which cover the wavelength range from 40 to 210 μm. Gallium-doped germanium detectors are proven to be very sensitive in the wavelength range of 40 to 120 μm. Application of ≈ 600 Nmm^{-2} of stress along the [100] crystallographic axis shifts the long wavelength cutoff from 120 μm to approximately 220 μm.[4]

Thus, we will use two Ge:Ga detector arrays, one stressed and one unstressed, to cover the desired wavelength range. The concentrations of Gallium dopants will be 1×10^{14} cm^{-3} and 2×10^{14} cm^{-3} for the stressed and unstressed arrays, respectively. The expected dark detector NEP is $\leq 5 \times 10^{-18}$ WHz$^{-1/2}$, which has been reached with a similar design in a balloon-borne experiment.[5] Some of the operational parameters of the detector arrays are listed in Tab. 1.

2. ARRAY DESIGN

The design for the stressed and unstressed detector arrays will be almost identical. For stability reasons, the *unstressed* detector array will actually be stressed to about 10 % of the long-wavelength stress level. As a tradeoff between sensitivity and susceptibility to cosmic rays, the size of the detector pixels was chosen to be roughly 1 mm^2 cross section with an interelectrode distance of 1.5 mm. Due to the high reflectivity and low absorption coefficient of Ge:Ga, the quantum efficiency of a free standing photoconductor would be very low. The probabilities for single pass absorption of a FIR photon by detectors this size are estimated to be 10 % and 20 % for unstressed and stressed Ge:Ga, respectively.[6] Therefore, the detectors are located in gold-plated integrating cavities with area-filling light cones to maximize the quantum efficiency. Electrically, the detector housing is maintained at a constant bias voltage, while the signal ends of the individual pixels are insulated from the housing by a thin shim of sapphire.

2.1. Finite Element Analysis

In order to optimize the stressing mechanism, we studied the stress distribution of a single detector pixel between two cylindrical steel pistons which apply an external force of 500 N, as shown in Fig. 1. Even in the case of a perfectly centred detector, the distribution of stress values within the detector is very inhomogeneous, with stress values varying between 405 and 765 Nmm^{-2}. This leads to a broadening of the spectral response curve and an enhanced probability of detector breakage. The stress uniformity within one pixel can be significantly improved by using a piston of a material with a higher Young's modulus or pedestals between the pistons and the detector. In our analysis, the use of silver pedestals reduces the variation of stress to a range of 486 to 507 Nmm^{-2}. As we see

Correspondence: rosenthal@mpe.mpg.de; phone: +49 - 89 - 3299 - 3362; FAX: +49 - 89 - 3299 - 3292

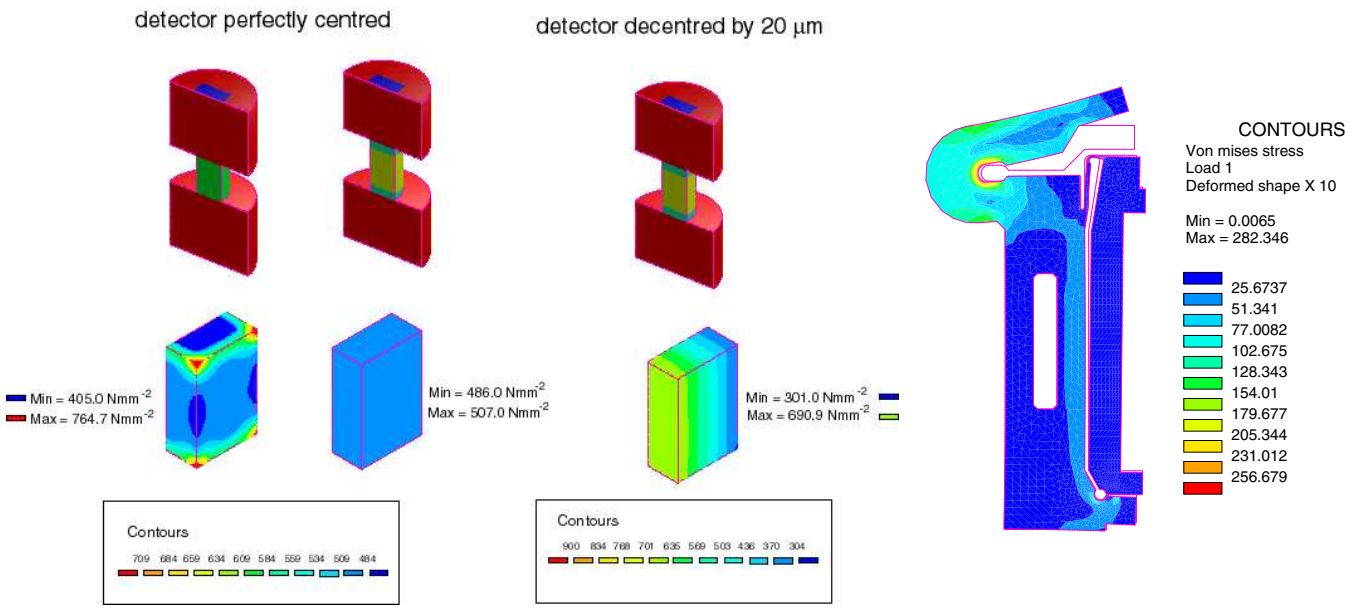

Figure 1. *Results of finite element analysis of one detector pixel between two cylindrical pistons in the case of a perfectly centred (left) and a 20 µm-decentred detector pixel for an external force of 500 N. Displayed is the stress distribution (in Nmm^{-2}) in the direction of the applied force. Also shown is the effect of a pedestal between the pistons and the detector. At right, the stress distribution of the detector housing is shown.*

Table 1. Parameters of the Detector Arrays

detector type	unstressed Ge:Ga	stressed Ge:Ga
wavelength range	40 – 120 μm	120 – 210 μm
size	16×25	16×25
bias field	10 – 20 Vm^{-1}	100 – 200 Vm^{-1}
operating temperature	1.8 K	3.5 K
doping concentration	$1 \times 10^{14} cm^{-3}$	$2 \times 10^{14} cm^{-3}$

from Fig. 1 (middle), the range of stress values is drastically increased if the detector is slightly (20 μm) decentred, which demonstrates the importance of precisely centred detectors. Although silver pedestals have been used, the stress values vary between 301 and 691 Nmm^{-2}.

On the right panel of Fig. 1, the stress distribution for the detector housing is shown. The highest stress levels occur at the "c-shaped" clamp, while the material near the detector stack remains unaffected.

2.2. Stressing Mechanism

Each detector is placed within about 20 μm of the centre of its cavity. As the finite element analysis (FEA) of the previous section has shown, this positional accuracy is required to avoid inhomogeneous stress, which would leadin to inhomogeneous responsivity and increased probability of pixel breakage. The edges of the detectors face the entrance holes of the cavities, to ensure that the first pass of reflected radiation is trapped by the integrating cavity and not reflected directly back out through the entrance aperture. The entire detector array will consist of 25 linear 1×16 pixel detector arrays, each equipped with its own linear light cone array. In Fig. 2, one linear stressed Ge:Ga detector array is sketched. The detector housing as well as the light cone arrays are machined by sparc erosion, which ensures high precision without introducing mechanical stress. As for the previous 5×5 FIFI detector array,[7,8] one screw at the top of the array serves as the stressing mechanism. To gradually increase the stress to the detectors when the stressing screw is turned, the horizontal slit is designed to create a spring mechanism. The spring constant

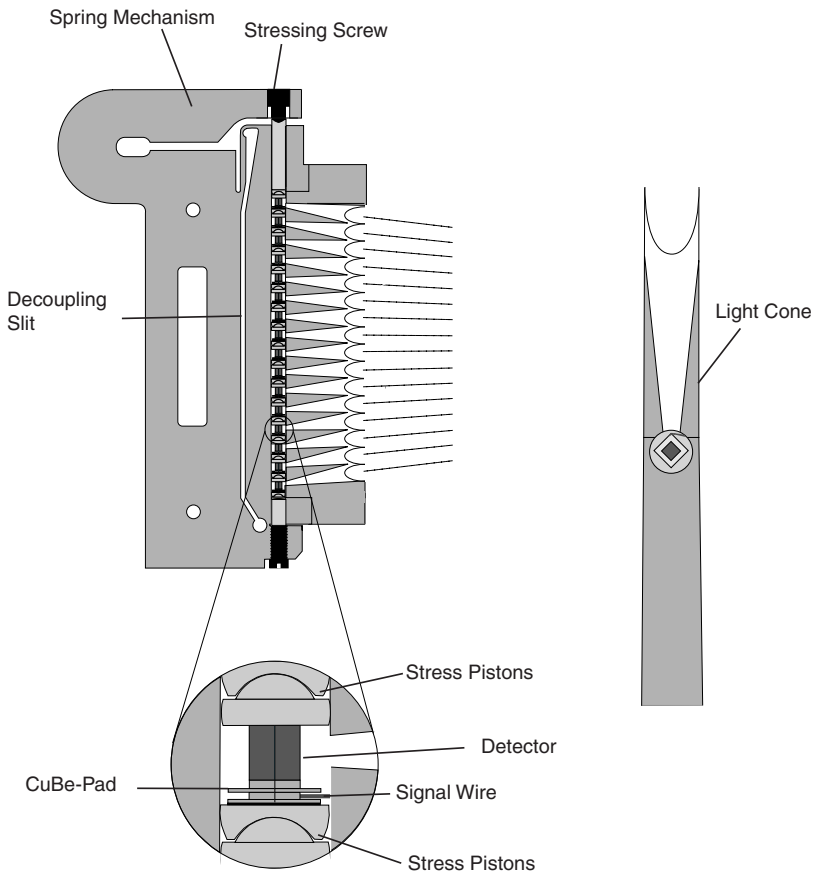

Figure 2. *Drawing of the detector housing of one 1 x 16 pixel linear stressed Ge:Ga array. The light cones are tilted in the focal plane to match the angle of incoming light from the pupil plane at a distance of 240 mm. The enlarged section shows a single detector cavity consisting of the detector, the combination of stress pistons, the CuBe pad, and the sapphire pad.*

at room temperature for the stressed detector array is $\approx$ 513 Nmm^{-1} and will be about $\approx$ 50 Nmm^{-1} for the unstressed array.

The detector housing is constructed of a high strength aluminum alloy (7075 Aluminum T6) which ensures a high mechanical stability and a good thermal conductivity. Due to a differential thermal contraction between the housing and the components of the detector stack, the stress to the detectors is increased during cool-down. For the stressed array, this increase is estimated to be about 100 N.

The vertical slit decouples the detector stack from any distortions caused by the stress application. The ball-and-socket pivot design of the tungsten carbide pistons compensates for non-parallel surfaces. To provide a uniform stress along the stack of detectors, the upper and lower parts of this combination are machined from spheres with diameter matching those of the detector cavities of 3 mm, so that they can rotate slightly without conducting forces into the housing. Due to the high Young's modulus of tungsten carbide, the bending of the pistons around the corners of the detectors is minimized. The signal end of a detector is in contact with the pedestal of a CuBe pad. Both the high Young's modulus of the tungsten carbide pistons and the pedestals of the CuBe pads lead to an improved stress homogenity within the pixels (see section 2.1). The CuBe pad is electrically insulated from the housing by a thin sheet of sapphire. The signal wire is soldered to the CuBe pad and led to the back end of the detector housing, where it is soldered to a connector. The connector is linked to the cryogenic readout electronics (CRE) located at the back of the detector housing.

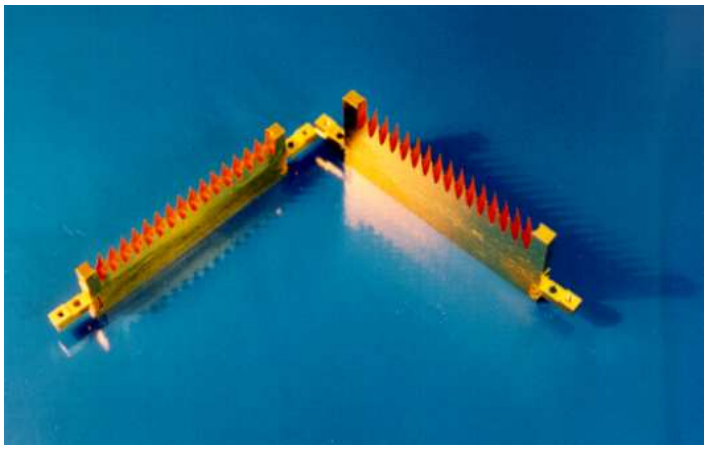

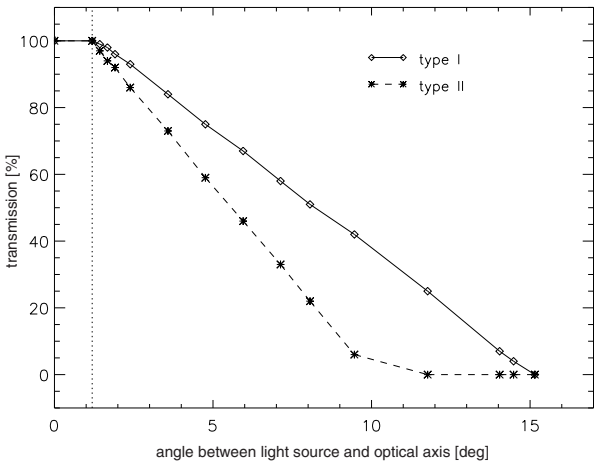

Figure 3. *left: Photograph of a prototype of the two types of light cones which are under study. right: Raytracing result to determine the transmission of the two types of light cones using the program "OptiCAD". The dotted line indicates the extent of the pupil. The transmission was determined by placing a point light source at a certain angle and counting the percentage of transmitted rays from a ray bundle which fully illuminated the entrance aperture of each light cone.*

Table 2. Parameters of the two types of light cones

	type I	type II
diameter of coupling hole	0.72 mm	0.5 mm
effective entrance hole[a]	3.6×3.6 mm^2	3.4×3.4 mm^2
length	19.9 mm	30.9 mm
distance to pupil[b]	240.1 mm	229.1 mm

[a] The circular entrance apertures of 5.1 and 4.9 mm diameter are cut to these square entrance apertures so as to completely cover the focal plane.
[b] Distance of aperture from the (previous) pupil.

2.3. Light Cones

To collect all of the light in the focal plane and to feed it into the appropriate detector cavity, funnel-shaped light cones are used. The back end of each linear light cone array forms a part of the integrating cavity (see Fig. 2). Like the cavities, the light cones are gold plated. The light cones are individually tilted in the focal plane to match the angle of incoming light from the pupil plane. Due to an easier and therefore cheaper production, we will use straight light cones which have been successfully used on the KAO with FIFI and not the parabolical Winston-type cones. In order to optimize the light cone arrays, we studied two different types of light cones (Fig. 3) whose parameters are listed in Tab. 2. Since the coupling holes are the main loss source of the detector cavities, we attempt to reduce their size as much as possible to optimize the quantum efficiency. On the other hand, the diameter of the coupling hole should be of order at least a few λ to minimize diffraction losses. To what extent type II with a coupling hole diameter of 0.5 mm is already affected by diffraction losses is not yet clear and has to be determined. On the right panel of Fig. 3, the simulated transmission for both types is plotted. Ray bundles from solid angles exceeding those of the pupil are no longer entirely transmitted, allowing the light cones to help reduce straylight. In this respect, type II is somewhat more efficient: it totally rejects light from light sources at angles $\geq 10^\circ = \alpha_{\rm cr}$ from the optical axis of the light cone, whereas $\alpha_{\rm cr} = 15$ for type I. However, this raytrace simulation uses geometrical optics and does not account for diffraction losses.

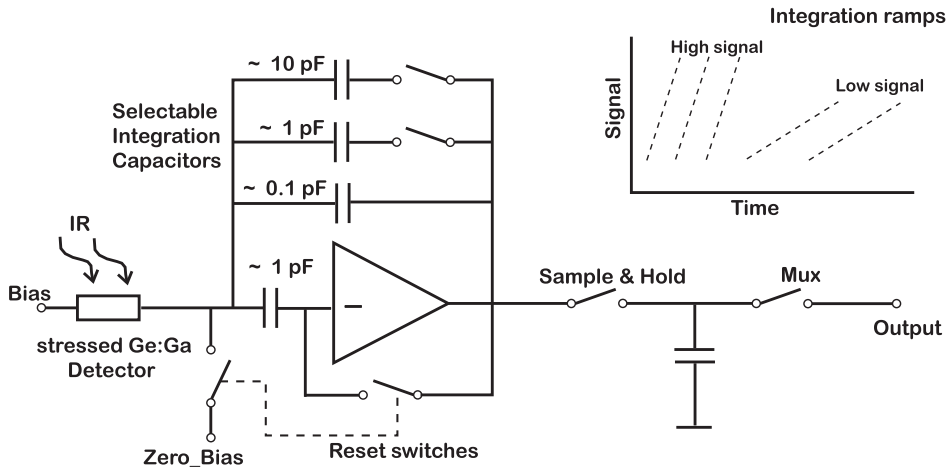

Figure 4. *Schematic of the cryogenic readout electronics (CRE).*

2.4. Readout Electronics

The purpose of the cryogenic readout electronics (CRE), together with some passive components, is to amplify and multiplex the signal of the 16 detectors of one linear array. The CRE is a specially designed CMOS circuit under development for FIRST-PACS,[9,10] operating at liquid helium temperature or lower (see Fig. 4). The detector current of each pixel is read out by an integrating amplifier. A sample-and-hold stage acts as analog memory between the integrator and the multiplexer circuit. All channels of one complete detector column are sampled at the same time and switched sequentially to the output of the CRE by the sample-and-hold circuit.

The complete read out of each 16×25 pixel photoconductor array is done by a 16-bit BiCMOS A/D converter stage. Very careful shielding, including output signal feedback on the shield, is used to minimize the load on the cryogenic output stage and the crosstalk between the analog signal lines to the converter stage. A digital multiplexer circuit provides parallel/serial conversion of the 16-bit data words generated by the A/D converter stage for both photoconductor arrays. The resulting 8 Mbit per second serial data stream (at 10 kHz maximum sampling rate) is transmitted to the data acquisition system via fiber obtics.

3. PERFORMANCE MEASUREMENTS

Several prototype linear 1×16 pixel arrays based on the above design have been succeessfully assembled and tested. A photograph of one of the assembled arrays is shown in Figure 5.

3.1. Stress Uniformity

To verify the functionality of the described stressing mechanism, we measured the room temperature resistance as a function of the applied stress, as shown in the left part of Fig. 6. The decrease of the resistance with increasing stress is very homogeneous along the stack of detectors, and no stress gradient is noticeable.

The relative spectral responses of four detectors at different positions within the stack measured with a Fourier-Transform Spectrometer (FTS) for a stress of 540 Nmm^{-2} also match quit well (Fig. 6). The cut-off wavelengths of the four detectors agree especially well.

3.2. Responsivity and Noise Equivalent Power

A setup of two blackbodies at 4 K and 20 K, one linear stressed detector array, and a Fabry-Perot interferometer, tuned to a centre wavelength of 170 μm at a resolving power of about 50, was used to measure the responsivity and NEP of the detectors.[11] The parameters were set to produce a photon power of 3×10^{-13} W per pixel which corresponds to the expected background with FIFI LS ($\lambda = 170$ μm, $\lambda/\Delta\lambda = 2000$) on SOFIA. Unfortunately, in our preliminary measurement the detectors received a photon background four times higher due to unwanted stray

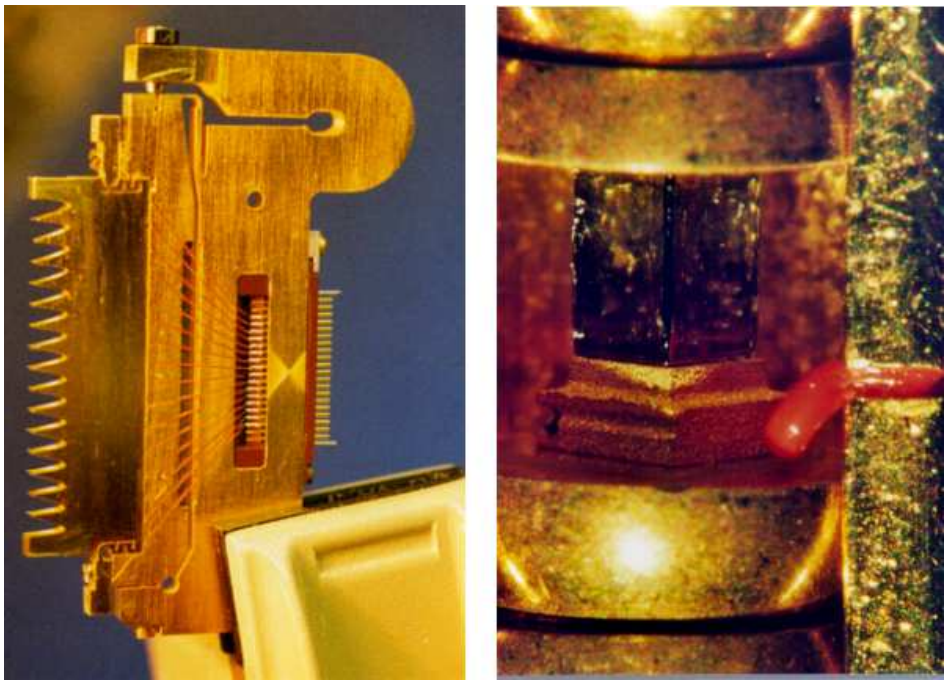

Figure 5. *Photograph of one prototype* 1×16 *linear detector array. On the left is the whole assembly, including the light cones, and on the right is a detailed view of one detector cavity.*

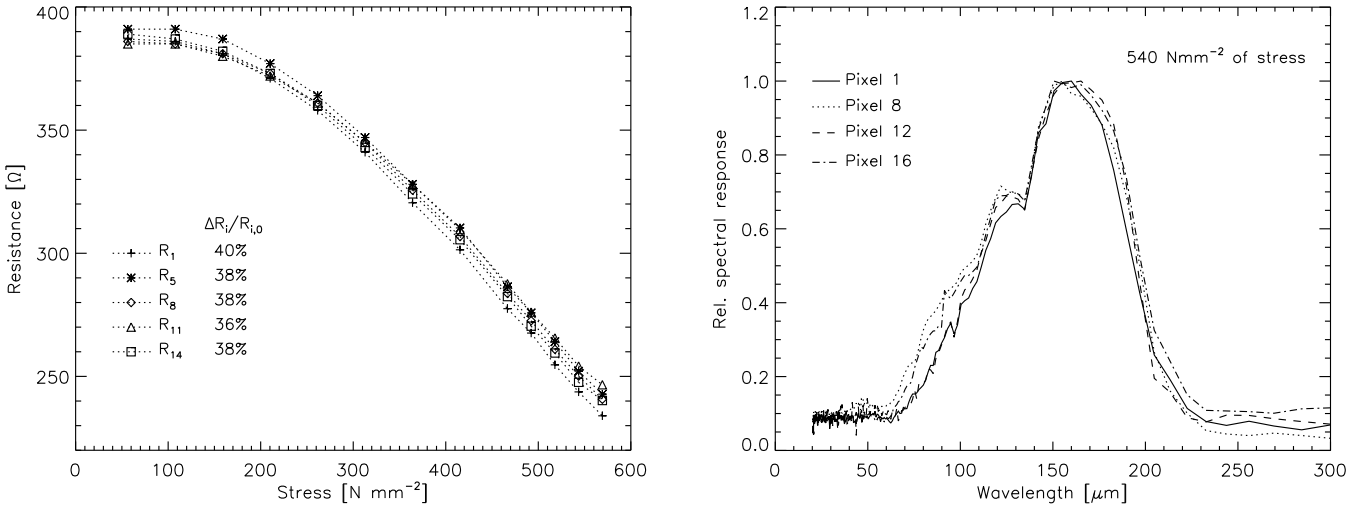

Figure 6. *left: Room temperature resistance as a function of the applied stress measured for five detectors of one linear array. The indices indicate the positions (counted from the stressing screw) of the detectors within the stack. right: Relative spectral response of four detectors measured at 2 K.*

light. Since we also lacked the readout electronics described in section 2.4, we used the transimpedance amplifiers (TIAs) with GaAs - FET's used for the FIFI array. With that, only a few detectors could be tested.

In Fig. 7 we compare the responsivity and NEP measured for our detectors and for the FIFI array, measured with narrow-band filters centred at 163 μm at a photon background of 2.39×10^{-13} W per pixel.[8] As shown in Fig. 7, the responsivity of our detectors at a given bias field is lower than for the FIFI array. However, as we see from the NEP measurement, this effect is effect is compensated by our ability to apply a higher bias field. The NEP

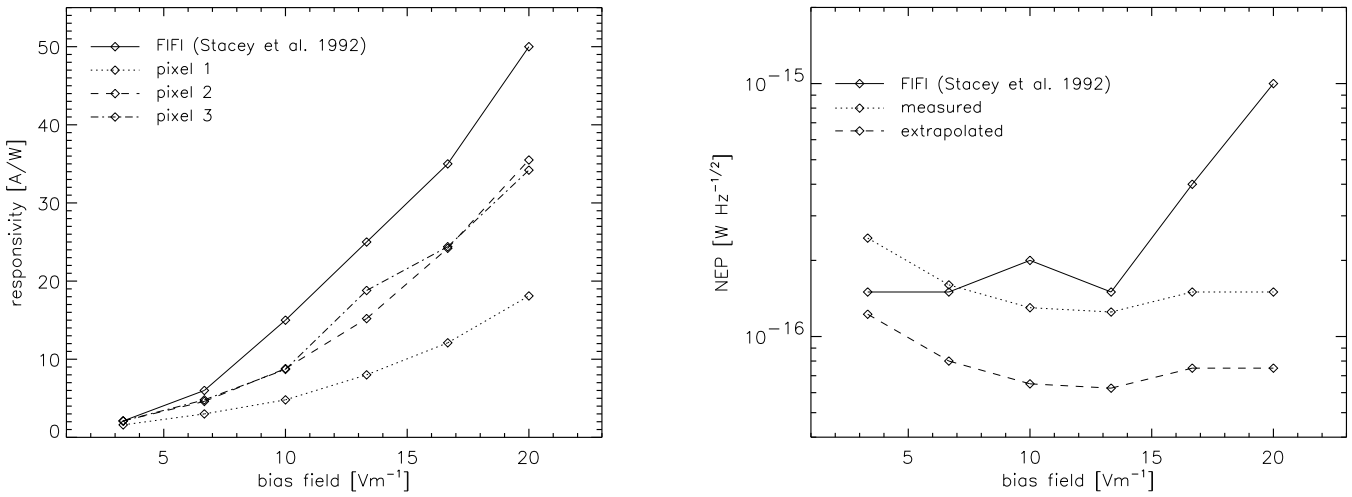

Figure 7. *Measured responsivity (left) and noise equivalent power (NEP, right) vs. the applied bias field for three detectors of one linear array compared with the performance of the FIFI detector array.*[8] *Using a 20 K blackbody as the light source, the Fabry-Perot spectrometer was tuned to a centre wavelength of 170 μm with a spectral resolution $\lambda/\Delta\lambda$ of $\approx$ 50, which produced a photon power of 3×10^{-13} W per pixel. Unfortunately, in our preliminary measurements the detectors received a background four times higher due to stray light. Under the assumption of background-limited performance, the measured NEP was therefore extrapolated to the lower background expected for FIFI LS ($\lambda = 170$ μm, $\lambda/\Delta\lambda = 2000$) on SOFIA.*

of the detectors is almost constant over the considered range of bias fields, whereas the NEP of the FIFI detectors rises steeply for bias fields $\geq$ 13 Vm^{-1} where impact ionization leads to increased noise.

Even with a background four times higher, above a bias field of about 7 Vm^{-1}, our measured NEP lies below that measured for the FIFI array. Under the assumption of a background-limited performance of the detectors and no noise contribution from the readout electronics, we extrapolated the measured NEP to the desired photon power of 3×10^{-13} W per pixel. The extrapolated NEP is well below that measured for the FIFI array, which may be due to the improved cavity design and the resulting enhanced quantum efficiency. The $NEP_{\rm BLIP}$ for background limited performance can be expressed as

$$NEP_{\rm BLIP} = \frac{h\nu}{\eta} \left(\frac{2^3 A\Omega}{\lambda^2} \Delta\nu t\epsilon\eta \, \frac{1}{1 - {\rm e}^{h\nu/kT}} \left(1 + t\epsilon\eta \, \frac{1}{1 - {\rm e}^{h\nu/kT}} \right) \right)^{1/2}, \qquad (1)$$

where t and ϵ are the transmission and emissivity of a blackbody at a temperature T, and η is the quantum efficiency of the detectors. With the measured NEP we used Eq. 1 to calculate a quantum efficiency $\eta = 45$ %, which is a substantial improvement over the average of 19 % reported for the FIFI detector array.[8]

The results of our first measurements are encouraging. However, we need more measurements on a larger number of detectors to confirm these first results.

ACKNOWLEDGMENTS

We are thankful to H. Dohnahlek and G. Kettenring for the design work, and to A. J. Baker for careful reading of the manuscript.

REFERENCES

1. Geis, N., Poglitsch, A., Raab, W., Rosenthal, D., Kettenring, G., Henning, T., & Beeman, J. in *Infrared Astronomical Instrumentation*, SPIE proc., Fowler, A. M. (eds.) 1998, p. 973

2. Raab, W., Geis, N., Looney, L., Poglitsch, A., Rosenthal, D., Urban, A., Henning, T. & Beeman, J. W. in *The International Symposium on Optical Science, Engeneering and Instrumentation*, SPIE proc., Fowler, A. M. (eds.) 1999, p. 973
3. Looney, L. W., Geis, N., Genzel, R., Park, W. K., Poglitsch, A., Raab, W., Rosenthal, D., & Urban, A. 2000, this volume
4. Kazanskii, A., Richards, P. L., & Haller, E. E. 1977, Ap. Phys. Lett., 31, 496
5. Hiromoto, N., Itabe, T., Argua, T., Okuda, H., Matsuhara, H., Shibai, H., Nakagawa, T., & Saito, T. 1989, IR Phys., 29, 255
6. Wang, J.-Q., Richards, P. L., Beeman, J. W., Haegel, N. M., & Haller, E. E. 1986, Appl. Optics, 25, 4127
7. Poglitsch, A., Beeman, J. W., Geis, N., Genzel, R., Haggerty, M., Haller, E. E., Jackson, J., Rumitz, M., Stacey, G. J., & Townes, C. H. 1991, Int. J. Inf. Mill. Wav., 12, 859
8. Stacey, G. J., Beeman, J. W., Haller, E. E., Geis, N., Poglitsch, A., & Rumitz, M. 1992, Int. J. Inf. Mill. Wav., 13, 1689
9. Dierickx, B., Seijnaeve, J., & Schefferin, D. in *Submillimetre and Far-Infrared Space Instrumentation*, Rolfe, E. J. (ed.), Proc. ESA Symposium ESA SP-388,1996, p. 61
10. Poglitsch, A., Waelkens, C., & Geis, N.in *The International Symposium on Optical Science, Engeneering and Instrumentation*, SPIE proc., Fowler, A. M.(eds.) 1999, p. 221
11. Urban, A., 1999, diploma thesis, Ludwig-Maximilians-Universität München